Poisson-Schrödinger and *ab initio* modeling of doped Si nanocrystals: Reversal of the charge transfer between host and dopant atoms

Torbjörn Blomquist* and George Kirczenow†
Department of Physics, Simon Fraser University, Burnaby, British Columbia, Canada V5A 1S6
(Received 30 July 2004; published 4 January 2005)

We present *ab initio* density functional calculations that show P (Al) dopant atoms in small hydrogen-terminated Si crystals to be negatively (positively) charged. These signs of the dopant charges are *reversed* relative to the same dopants in bulk Si. We have therefore developed a self-consistent Poisson-Schrödinger model that allows us to bridge these two regimes of different charge character. Our Poisson-Schrödinger model is based on a nonorthogonal tight-binding model that reproduces the band structure of silicon very well, and we have also developed parameters for P, Al, and H. Using this model, we predict this reversal of the dopant charge to occur at crystal sizes of the order of 100 Si atoms. We explain it as a result of the competition between fundamental principles governing charge transfer in bulk semiconductors and molecules. Based on these general considerations, we expect it to occur in nanocrystals of most semiconductors. We also calculate band-edge energies and dopant-level energies for a number of crystallites containing 29–888 Si atoms.

DOI: 10.1103/PhysRevB.71.045301 PACS number(s): 73.22.−f, 71.15.−m

I. INTRODUCTION

The exponential increase of the speed and capacity for semiconductor technology, described by Moore's law,[1] has been enabled through continued miniaturization. Each generation of semiconductor technology has a 30% smaller length scale than the previous. Today, state-of-the-art semiconductors have a feature size of 90 nm. To continue this miniaturization further, it is important to understand the properties of semiconductors on the nanoscale where quantum effects become prominent.

Introducing appropriate impurity atoms (known as "dopants") into a semiconductor can increase the electrical conductivity by many orders of magnitude.[2,3] By doping a semiconductor, we can engineer its electrical properties—i.e., its conductivity and whether the current is mediated by electrons or holes. Doping is key to the operation of modern electronic devices. It is therefore important to understand the effects of the doping of semiconductor nanocrystals.

A semiconductor has, in the ground state, a valence band completely filled with electrons and a conduction band which is completely empty. The semiconductor cannot conduct current in this state; to conduct, one has either to add electrons to the conduction band or remove electrons from the valence band so that holes form there. Thermal excitation of electrons from the valence band to the conduction band is not possible for most semiconductors at room temperature. A substitutional impurity with one valence electron more than the host semiconductor is called a donor because if the donor is thermally ionized, the extra electron will be promoted to the conduction band and can freely move throughout the semiconductor crystal. Similarly an impurity with one valence electron fewer than the host is called an acceptor because it can accept an electron excited from the valence band, forming a hole. A donor (acceptor) is called shallow if the energy required to excite an electron (hole) from the impurity state to the conduction- (valence-) band edge is small, making thermal excitation possible at room temperature. The ground states for shallow donors and acceptors in bulk semiconductors such as silicon have been thoroughly studied.[3–9] The extra electron of a donor such as phosphorus in silicon will occupy a hydrogenlike orbital, extended to a radius of several lattice constants due to the reduced effective mass of the electron and dielectric shielding of the semiconductor host. The Bohr radius of this hydrogenlike orbital can be computed in the effective mass approximation[10] to be 30 Å,[3] which is very large compared to the atomic scale; consequently, the (negative) charge of the donor electron will be spread out over a large number of atoms, leaving the donor atom positively charged and the surrounding atoms negatively charged. In the case of an acceptor such as aluminum in silicon, the acceptor hole will also be very spread out, leaving the donor atom negatively charged, while the surrounding atoms will be positively charged. This qualitative picture of charge transfer between semiconductor host and shallow dopant is well established for bulk semiconductor materials and is fundamental to our understanding of the properties of semiconductor devices. Recent experimental and theoretical work[11–19] has shown that it also holds for a variety of doped semiconductor nanoparticles.

Chemistry offers a very different view of the charge transfer between atoms. Here it is instead driven by the electronegativity of the atom species—i.e., the ability of the atom species to attract extra (negative) charge.[20] Atoms with nearly filled valence shells have a large electronegativity because filled shells are energetically stable. Conversely an atom species with nearly empty valence shell will have a low electronegativity and will prefer to lose electrons to achieve a state without a partially filled valence shell. Simple semiconductors such as silicon have exactly half-filled valence shells. A donor atom, such as phosphorus, has one more valence electron and will thus have a larger electronegativity than silicon and be negatively charged. The chemical view therefore predicts quite the opposite charge-transfer effect from conventional semiconductor theory. Similarly an acceptor such as aluminum in silicon, which has one electron

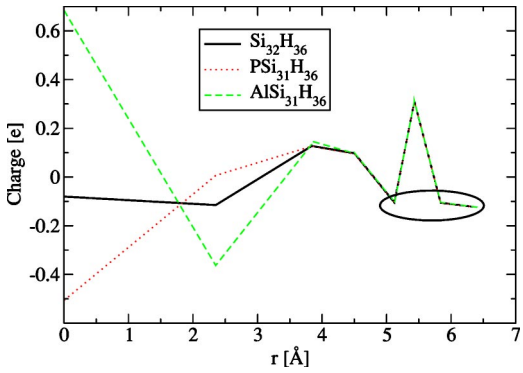

FIG. 1. (Color online) On-site natural population (Ref. 22) charge as function of the site's radial coordinate for $Si_{35}H_{36}$. The solid curve shows undoped crystallite. The dotted curve shows charge distribution when the central atom ($r=0$) has been substituted for phosphorus (donor in bulk) and the dashed curve shows the result for aluminum substitution (acceptor in bulk). The ellipse shows which atoms are hydrogen.

fewer than the host, will have a smaller electronegativity and become positively charged, again in contrast to conventional semiconductor theory.

The chemical view is well established for molecules and the semiconductor theory is well established for bulk semiconductors. We have performed *ab initio* density functional theory (DFT) calculations[21] on small hydrogen-terminated doped silicon crystallites, which confirm the chemical view, illustrated by Fig. 1, which shows the charge distribution in doped and undoped crystals, calculated using natural orbital population analysis. Calculating charge distributions in a nonorthogonal basis are nontrivial; one of the more accurate ways to handle the nondiagonal parts of the charge distribution is by using natural atomic orbitals (NAO's).[22] NAO populations are calculated by performing a basis transformation to an orthogonal basis with occupancy-weighted minimum deviations from the parent basis. High-accuracy *ab initio* density functional theory calculations using large basis sets, such as the one used here, can unfortunately not be used with very large crystals due to the practical limitations of computers. We have therefore developed a self-consistent Poisson-Schrödinger model based on a tight-binding model, which reproduces the band structure of silicon very well, in order to unify the chemical and bulk semiconductor regimes and study the crossover between them. We present in this article results for energy levels and charge distributions, while earlier work on semiconductor nanocrystals has mainly focused on optical properties.[23,24]

II. NONORTHOGONAL TIGHT-BINDING MODEL

Our Poisson-Schrödinger model for silicon is based on a tight-binding (TB) model developed by Bernstein *et al.*,[25] hereafter referred to as the Bernstein model. We have chosen this model because it reproduces the band structure of silicon very well. We have modified the Bernstein model in the following ways: Bernstein's on-site potentials are functions of the local density of atoms; we instead make it a function of orbital occupation, using valence orbital ionization energies (VOIE's).[26] The reason for this change is that we want a self-consistent model. Our on-site energies have been chosen to agree with Bernstein's in the case for bulk silicon, in order to preserve the band structure. The on-site potential of an orbital of type $l \in \{s,p,d\}$ on site i is given as

$$h_{il} = A_l p_{il} + B_l + C_l q_i + V_i, \tag{1}$$

where A_l, B_l, and C_l are fitting parameters, given in Table I, $0 \leqslant p_{il} \leqslant 2$ is the population of the orbital, q_i is the total charge on the atom, and V_i is the electric potential at the site. See Appendix A for how to calculate V_i. The distance-dependent part of the two-center Hamiltonian matrix elements is given by[25]

TABLE I. On-site parameters. The A and C parameters for s and p orbitals are taken from VOIE's, while the values for d orbitals are estimates, based on parameters from sulfur ($C_d=0.64C_p$ and $A_d=0$) since no VOIE was available. The B parameters for Si have been chosen so the on-site energies coincide with Bernstein's parameters for bulk Si. The B parameters for Al and P have been fitted to produce reasonable charge distributions for small doped crystals.

Orbital	A (Ry)	B (Ry)	C (Ry/e)
Si-s	0.12201	−0.322132	−0.59460
Si-p	0.08232	0.352257	−0.59460
Si-d	0.0	1.08175	−0.37999
Al-s	0.10584	−0.0919849	−0.52331
Al-p	0.08305	0.576522	−0.52331
Al-d	0.0	1.15528	−0.33442
P-s	0.14626	−0.586838	−0.65781
P-p	0.08305	0.212551	−0.65781
P-d	0.0	1.00822	−0.42041

TABLE II. Some properties of the tight-binding model (Ref. 25). Experimental values are given in parentheses (Ref. 29).

Position of conduction-band minima	87.7% Γ-X	(85%)
Band gap	1.01 eV	(1.12)
Light-hole mass	$0.26m_e$	(0.15)
Heavy-hole mass	$0.31m_e$	(0.54)
Longitudinal electron mass	$0.55m_e$	(0.92)
Transverse electron mass	$0.15m_e$	(0.19)

$$H_{ll'\mu}(R) = (a_{ll'\mu} + b_{ll'\mu}R + c_{ll'\mu}R^2)e^{-g_{ll'\mu}^2 R}f(R), \quad (2)$$

where $\mu \in \{\sigma, \pi, \delta\}$ denotes the type of interaction between the two orbitals of type l and l', and $a_{ll'\mu}$, $b_{ll'\mu}$, $c_{ll'\mu}$, and $g_{ll'\mu}$ are fitting parameters found in Ref. 25. The cutoff function $f(R)$ is given by

$$f(R) = \begin{cases} \left[1 + \exp\left(\dfrac{R - R_c + 5L_c}{L_c}\right)\right]^{-1}, & R \leqslant R_c, \\ 0, & R > R_c, \end{cases} \quad (3)$$

where $R_c = 12.5$ a.u. and $L_c = 0.5$ a.u. The distance-dependent part of the overlap matrix elements is[27]

$$S_{ll'\mu}(R) = (\delta_{ll'} + t_{ll'\mu}R + q_{ll'\mu}R^2 + r_{ll'\mu}R^3)e^{-u_{ll'\mu}^2 R}f(R), \quad (4)$$

where $t_{ll'\mu}$, $q_{ll'\mu}$, $r_{ll'\mu}$, and $u_{ll'\mu}$ are fitting parameters found in Ref. 25. The angular dependence of the Hamiltonian and overlap matrix elements is the standard two-center Slater-Koster form.[28] Some properties of this model are given in Table II; see also the band structure in Fig. 2.

Since aluminum and phosphorus are isoelectronic, we use the same hopping and overlap parameters as for silicon. The on-site energies however are based on VOIE data, together with a fit for the B_l parameters; see Table I. See also Appendix B.

For hydrogen we use an s basis with the on-site potential

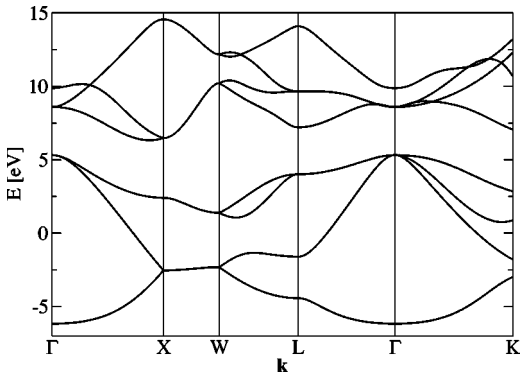

FIG. 2. Band structure of silicon, calculated in the present model.

$$h_i = 0.008893q_i^3 - 1.026776q_i^2 - 1.979317q_i + 0.232 + V_i, \quad (5)$$

expressed in Ry and based on valence orbital ionization energy for the charge dependence;[26] the value 0.232 is a fitted parameter (see Appendix B). The distance-dependent part of the two-center Hamiltonian between the hydrogen s orbital and an l-type orbital in silicon is taken to be

$$H_{sl}(R) = \frac{s_l d_0^2}{R^2} f(R), \quad (6)$$

where $d_0 = 2.80$ a.u. is the bond distance, and $s_s = -0.49$, $s_p = -0.23$, and $s_d = 0$ are fitting parameters. The hydrogen orbitals have been assumed to be orthogonal to all silicon orbitals; choosing nonzero overlap matrix elements does not improve the fit noticeably.

To complete the Poisson-Schrödinger model, we self-consistently solve the tight-binding model and the electrostatic potential by populating all the states below the Fermi level with electrons. For nonzero temperature, a Fermi-Dirac distribution may be used. The details of how the electrostatic potential is calculated can be found in Appendix A. Our model is similar to the one used by Lannoo *et al.*[13]

III. RESULTS

We have applied the present model to calculate the ground-state properties of a number of silicon nanocrystals ranging in size from $Si_{29}H_{36}$ to $Si_{888}H_{372}$, with and without dopants. The crystallites are constructed from a diamond lattice by taking all atoms inside a sphere centered on one of the lattice sites. The surface of the crystallite is treated by first removing all silicon atoms that have only one bond with the crystallite. The crystallite is then hydrogen terminated by attaching hydrogen atoms to the surface silicon atoms at what would have been neighboring silicon sites and the silicon-hydrogen bonds are shortened to 1.48 Å (the bond length in SiH_4). Hydrogen termination is important to obtain a clean energy gap.[30] These crystallites have tetrahedral symmetry. We have also studied the effects of surface reconstructions by mimicking the reconstruction of a $Si(100)2\times1$:H surface[31] where it is appropriate. The geometry of these reconstructions is based on an *ab initio* DFT calculation.[21] The reconstruction of the surface often breaks the tetrahedral symmetry of the crystallites, with important implications for the degeneracy of dopant states. The doped crystals have the central silicon site substituted with aluminum or phosphorus.

Figure 3 shows how the energies of the valence- and conduction-band edges change with nanocrystal size and also the effects of surface reconstructions. The conduction-band-edge energy varies little with nanocrystal size. The valence-band edge moves up, narrowing the band gap to ~1.5 eV for $Si_{888}H_{372}$ (largest nanocrystal) from ~2.7 eV for $Si_{29}H_{36}$ (smallest nanocrystal). The surface reconstructions increase the energies of both the conduction- and valence-band edges, while the band gap remains approximately unchanged.

The band gap can be fitted to a function

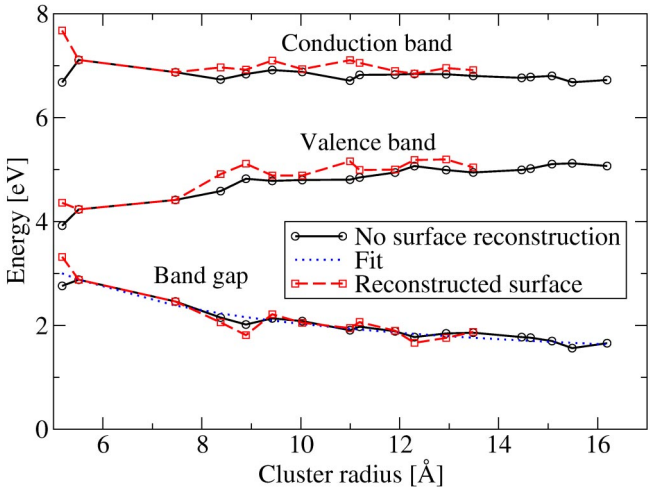

FIG. 3. (Color online) The valence-band-edge and conductance-band-edge energies, as well as the band gap of the different undoped crystallites as function of crystallite radius. Solid lines and circles show energies for crystals with unreconstructed surfaces. Dashed lines and boxes show energies for crystals with surface reconstructions. The dotted line is a fit of the function $E_g(r)$ for comparison with Refs. 30 and 32.

$$E_g(r)/E_{g0} - 1 = Ar^{-b}, \tag{7}$$

where $r = 1.685N^{1/3}$ is the radius of the crystallite, N is the number of Si atoms, E_{g0} is the band gap in the bulk, and A and b are fitting parameters. We find that $A = 10.5$ and $b = 1.0$; see fitted line in Fig. 3. Liu *et al.*[30] and Zunger *et al.*[32] report $b = 1.37$ in models without Coulomb interactions. Effective mass theory (particle in a box) predicts an r^{-2} scaling. Our result, however, agrees very well with density functional theory calculations.[12,33,34] Although we have the same power scaling as DFT calculations for the band gap, we do not have the same absolute magnitude (not the same A): Our silicon parameters are optimized for a correct band gap for bulk silicon, but our hydrogen parameters have been fitted to reproduce the DFT charge distribution in small crystals, not the band gap. We therefore do not get exactly the same confinement effect on the band gap as DFT. We note, however, that there is still disagreement in the literature as to what the gap is in these crystals, with quantum Monte Carlo calculations differing substantially from DFT.[35]

There has been interest in how the system size affects the dopant levels, and there have been a number of studies using different methods—for example, effective mass theory,[14–16] TB,[16,17] partial retention of diatomic differential overlap (PRDDO),[18] and DFT.[19] We define the dopant level as the energy difference between the partly filled single-particle dopant eigenstate and its nearest-neighbor eigenstate. Studying the crystallites without surface reconstructions (see Fig. 4), we see that the Al dopant levels vary quite smoothly with crystal size. We have fitted the function

$$E_d(r) = A/r^2 + B \tag{8}$$

to the dopant-level energies, with parameters $A = 14$ eV Å^2 and $B = 0.112$ eV. The experimental bulk value for an Al dopant in silicon is 69 meV.[29] Extrapolating to infinite crystal size, we see that our model produces a somewhat too large, but still very reasonable dopant level for aluminum. For crystals with surface reconstructions, the tetrahedral geometry is broken and the dopant level, which in the case for aluminum was threefold degenerate, is split. The splitting is very small and poses problems both for interpretation of what the dopant-level energy should be (see our definition of dopant energy level above) and for the convergence of the calculations (an energy splitting of less than 3 meV near the Fermi level at 0 K poses a problem; this can be remedied by increasing temperature to 30–100 K). The P dopant levels, as opposed to Al, vary a lot from crystal to crystal. It is not reasonable to try to fit a function in this case, but we note that the largest crystallites studied in our calculations produce dopant energy levels near the experimental value 46 meV.[29] We attribute the difference in behavior between the acceptor and donor states to the fact that the electron states have a larger probability on the surface sites, making donor states much more sensitive to the surface than acceptor states which typically are more localized to the interior of the crystal; see the bottom graphs of Figs. 5 and 6. The introduction of surface reconstructions to the P-doped crystals does not cause the same problems as with Al as generally the donor ground states are not degenerate, but the donor states' sensitivity to the surface still causes large changes. The general behavior shown for unreconstructed crystals in the bottom graph of Fig. 4 is, however, not changed by the reconstructions (not shown). The strong variations for the donor-state levels suggest that it would be difficult to engineer the properties of a small n-doped crystal without atomic control in the manufacturing. It is also relevant in this regard that the bands in these small structures are made up from discrete energy levels, and even for our largest crystallites, these levels have an energy spacing of 5–50 meV.

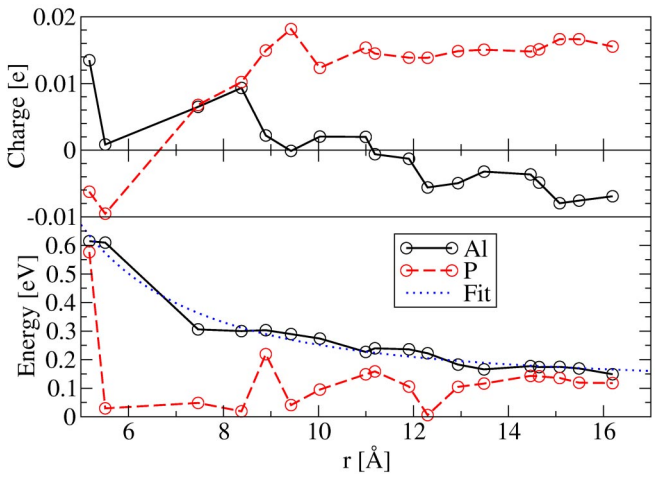

FIG. 4. (Color online) The top graph shows the charge on the dopant site for different Al- (solid line) and P- (dashed line) doped crystals as function of crystal radius. The bottom graph shows the energy of the dopant state for the same crystals. A fit $E_d(r) = A/r^2 + B$ to the Al-dopant energies is shown (dotted line).

The charge on the impurity site for the phosphorus-doped crystallites (see Fig. 4 and the $r = 0$ position in top graph of

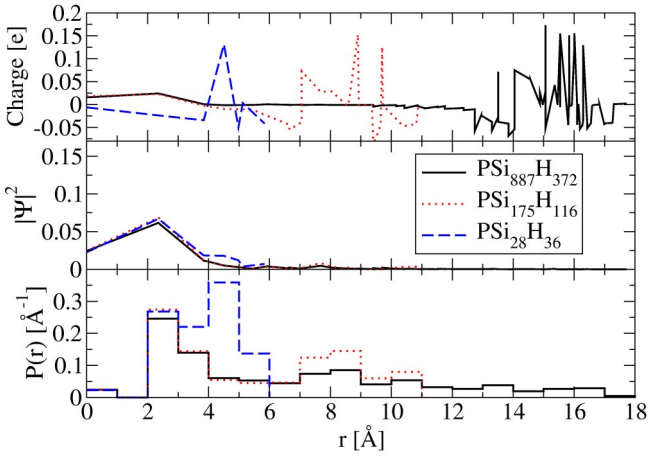

FIG. 5. (Color online) Top graph: total Mulliken charge on each site as function of radial coordinate for three different P-doped crystals. The charge distributions are generally very symmetric. Center graph: Mulliken probability distribution for the donor single-particle eigenstate. Bottom graph: radial probability distribution for the dopant state, calculated by dividing the radial coordinate into bins.

Fig. 5) exhibits a crossover from negative to positive when going from small to large nanocrystals. This crossover between the quasimolecular behavior and bulk semiconductor behavior occurs between $PSi_{34}H_{36}$ and $PSi_{86}H_{76}$. For the aluminum-doped crystallites (Figs. 4 and 6) we find a crossover from a positive to a negative impurity site between $AlSi_{147}H_{100}$ and $AlSi_{292}H_{172}$. The precise crossover points are sensitive to the parameters of the model, and this result should be regarded as a first (order of magnitude) estimate. The charges on the impurity site in Figs. 5 and 6 are consistently somewhat smaller in magnitude than in Fig. 1; we attribute this difference to the fact that Mulliken population analysis (Figs. 5 and 6) tends to smear the charge between overlapping orbitals on neighboring atoms more than do natural orbital calculations (Fig. 1). Mulliken population analysis is the simplest way to calculate charge in a nonorthogonal basis; a nondiagonal element of the charge matrix is simply equally distributed between the pair of overlapping orbitals. The experimental VOIE parameters used in our model are optimized for use with Mulliken population analysis.

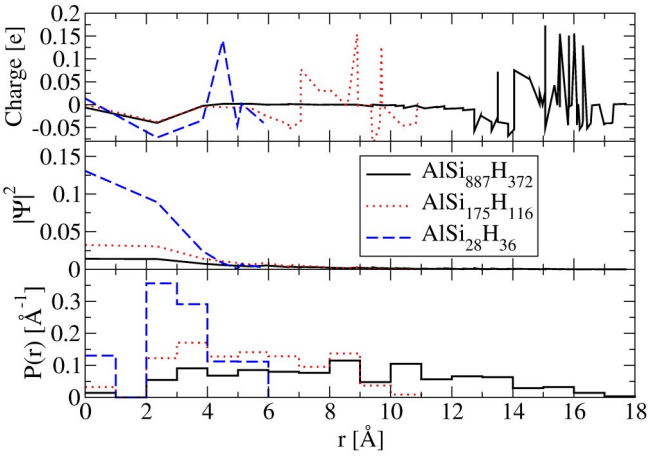

FIG. 6. (Color online) Top graph: total Mulliken charge on each site as function of radial coordinate for three different Al-doped crystals. The charge distributions are generally very symmetric. Center graph: Mulliken probability distribution for the acceptor single particle eigenstate. Bottom graph: radial probability distribution for the dopant state, calculated by dividing the radial coordinate into bins.

The dopant site charge (see Fig. 4) cannot be explained in a simple way in terms of dopant-level energies, band-gap energies, or band-edge energies (see Fig. 3); detailed self-consistent calculations are required for reliable predictions.

The dielectric response to the impurity obviously changes with crystal size, since the charge on the impurity changes; this shows the importance of performing a self-consistent calculation. One-electron (or -hole) models[14–16] that have been used to treat dopants in quantum dots can therefore not be extended to the nanoscale as the effective impurity potential changes.

IV. CONCLUSIONS

We have developed a self-consistent Poisson-Schrödinger model[36] based on a nonorthogonal tight-binding model.[25] The present model reproduces the band structure of silicon very well, and we have developed parameters also for hydrogen, phosphorus, and aluminum in order to explore the properties of doped and hydrogen-terminated silicon nanocrystals. Our model has allowed us to explore the crossover from a previously unexplored regime in semiconductor nanocrystals in which the molecular view of charge transfer between atoms holds true to a regime where macroscopic solid-state semiconductor theory prevails. The crossover is signaled by a striking reversal of the sign of the charge transfer between the host semiconductor and dopant atom that has not been anticipated in previous experimental or theoretical work. We predict that it should occur at nanocrystal sizes of the order of 100 Si atoms. The charge reversal is not related in a simple way to the band gap or the dopant energy levels of the crystallites. Since very basic principles of solid-state semiconductor physics and molecular chemistry are the underlying reasons for the charge reversal, we predict it to be a general phenomenon occurring for a wide variety of nanoscopic semiconductors and dopants. The charge crossover also shows the importance of using a self-consistent model since one-electron (or -hole) models does not include the change in dielectric response to the impurity with crystal size.

For Si nanocrystals we find an energy gap widening that scales as $r^{-1.0}$ consistent with density functional theory calculations.[12,33,34] We predict that the dopant energy level for Al in Si crystallites varies smoothly and can be fitted to a function $E_d(r)=A/r^2+B$ where B is the dopant level in bulk silicon. Donor levels should vary widely from crystallite to crystallite, making it difficult to engineer properties of P-doped Si nanocrystals without atomic control in manufacturing.

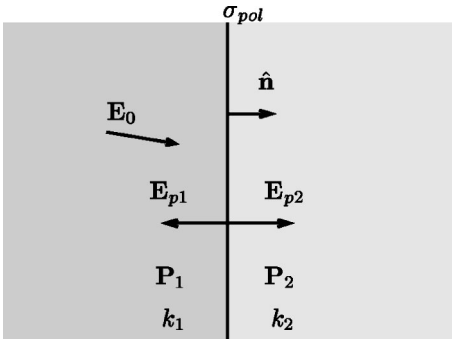

FIG. 7. Interface between two dielectric media with dielectric constants k_1 and k_2. $\mathbf{E}_0$ is an applied electric field that induces polarization $\mathbf{P}_1$ and $\mathbf{P}_1$ of two the media. The polarization causes a surfaces charge density σ_{pol} at the surface and electric fields $\mathbf{E}_{p1}$ and $\mathbf{E}_{p1}$ normal to the surface.

ACKNOWLEDGMENTS

This work was supported by NSERC and the Canadian Institute for Advanced Research.

APPENDIX A: ELECTROSTATIC INTERACTION

This appendix describes how the electrostatic potential in the structure is calculated, taking into account the polarization of the core electrons of silicon. The electrostatic potential at a site would, in the simplest case, be the sum of Coulomb potentials from all other sites plus an on-site contribution included in Eq. (1). Our tight-binding model, however, only includes valence electrons but core electrons will also contribute to the potential through dipole interaction. We chose to view the silicon crystallite as a macroscopic medium with a dielectric constant k_c relating to the polarization of the cores. To do this, we have to define a surface and calculate the surface polarization charge.

1. Polarization charge

We calculate the polarization charge density σ_{pol} at an interface between two different media with dielectric constants k_1 and k_2 as a response to an applied electric field $\mathbf{E}_0$ (see Fig. 7).[37] The electric field $\mathbf{E}_0$ can be from point charges or other parts of the polarization surface. In the case of the point charges, we have a local response from the dielectric medium, shielding the charge to an effective value of q/k_r where k_r is the local dielectric constant. The dielectric medium produces charge density only near sources and near surfaces and interfaces, so we need only to concern ourself with these points.

There will be an electric field

$$E_p = \frac{\sigma_{pol}}{2\epsilon_0} \tag{A1}$$

from the polarization surface, directed as

$$\mathbf{E}_{p1} = -E_p\hat{\mathbf{n}}, \quad \mathbf{E}_{p2} = E_p\hat{\mathbf{n}} \tag{A2}$$

in the two media (see Fig. 7). The polarization in the two media is

$$\mathbf{P}_i = (\mathbf{E}_0 + \mathbf{E}_{pi})\epsilon_0(k_i - 1). \tag{A3}$$

The surface polarization charge density is given by

$$\sigma_{pol} = (\mathbf{P}_1 - \mathbf{P}_2)\cdot\hat{\mathbf{n}}, \tag{A4}$$

where $\hat{\mathbf{n}}$ is a surface normal. Equations (A1)–(A4) allow us to calculate the surface polarization charge as

$$\sigma_{pol} = 2\epsilon_0\mathbf{E}_0\cdot\hat{\mathbf{n}}\frac{k_1 - k_2}{k_1 + k_2}. \tag{A5}$$

The electric field can be written as

$$\mathbf{E}(\mathbf{r}) = \sum_j \frac{q_j(\mathbf{r} - \mathbf{r}_j)}{4\pi\epsilon_0 k_j|\mathbf{r} - \mathbf{r}_j|^3} + \int_S d\mathbf{r}'\frac{\sigma_{pol}(\mathbf{r}')(\mathbf{r} - \mathbf{r}')}{4\pi\epsilon_0|\mathbf{r} - \mathbf{r}'|^3}, \tag{A6}$$

where q_j are point charges at positions $\mathbf{r}_j$ where the medium has dielectric constant k_j and S is the interface between the two media. We discretize the surface S in order to compute the surface charge,

$$\int_S d\mathbf{r}' \to \sum_l \mathbf{S}_l, \tag{A7}$$

where $\mathbf{S}_l = S_l\hat{\mathbf{n}}_l$ are discrete area elements with normal vectors defined in the direction from media 1 to media 2; the area elements are centered at coordinates $\mathbf{r}_l$. This assumes that the field $\mathbf{E}(\mathbf{r})$, which we will be integrating, is approximately constant over the surface element $\mathbf{S}_l$, which is not always true; we must therefore make an exception for when we consider the field $\mathbf{E}_l(\mathbf{r}_l)$ from a point charge at $\mathbf{r}_l$. We will want to conserve the total flux from the point charge; exactly half the flux from the point charge will go through the surface element $\mathbf{S}_l$ when the position of the point charge approaches the surface,

$$\int_{S_l} dS\mathbf{E}_l(\mathbf{r}) = \frac{q_l}{2k_l\epsilon_0}, \tag{A8}$$

which allows us to define an effective and average electric field at $\mathbf{r}_l$:

$$\mathbf{E}_l(\mathbf{r}_l) = \frac{q_l\hat{\mathbf{n}}_l}{2k_l\epsilon_0 S_l}. \tag{A9}$$

We can now write the electric field, Eq. (A6), as

$$\mathbf{E}(\mathbf{r}_i) = \sum_{j\neq i} \frac{q_j(\mathbf{r}_i - \mathbf{r}_j)}{4\pi\epsilon_0 k_j|\mathbf{r}_i - \mathbf{r}_j|^3} + \frac{q_i\hat{\mathbf{n}}_i}{2k_i\epsilon_0 S_i} \tag{A10}$$

$$+ \sum_{l\neq i} \frac{q_l^{pol}(\mathbf{r}_i - \mathbf{r}_l)}{4\pi\epsilon_0|\mathbf{r}_i - \mathbf{r}_l|^3} + \frac{q_i^{pol}\hat{\mathbf{n}}_i}{2\epsilon_0 S_i}, \tag{A11}$$

where

$$q_l^{pol} = \sigma_{pol}(\mathbf{r}_l)S_l = 2\epsilon_0\mathbf{E}(\mathbf{r}_l)\cdot\mathbf{S}_l\frac{k_1 - k_2}{k_1 + k_2}. \tag{A12}$$

We obtain an equation for q_i^{pol},

$$q_i^{pol} = \frac{k_1 - k_2}{k_1 + k_2}\left(\sum_{j\neq i}\frac{q_j(\mathbf{r}_i - \mathbf{r}_j)\cdot\mathbf{S}_i}{2\pi k_j|\mathbf{r}_i - \mathbf{r}_j|^3} + \frac{q_i}{k_i} + \sum_{l\neq i}\frac{q_l^{pol}(\mathbf{r}_i - \mathbf{r}_l)\cdot\mathbf{S}_i}{2\pi|\mathbf{r}_i - \mathbf{r}_l|^3} + q_i^{pol}\right), \tag{A13}$$

which we can turn into the matrix equation

$$(I - B)\mathbf{q}_{pol} = A\mathbf{q}, \tag{A14}$$

where I is the identity matrix, by performing the definitions

$$(\mathbf{q}_{pol})_i = q_i^{pol}, \tag{A15}$$

$$(\mathbf{q})_i = q_i, \tag{A16}$$

$$(A)_{ij} = \frac{k_1 - k_2}{k_1 + k_2}\times\begin{cases}\dfrac{(\mathbf{r}_i - \mathbf{r}_j)\cdot\mathbf{S}_i}{2\pi k_j|\mathbf{r}_i - \mathbf{r}_j|^3}, & i\neq j,\\ 1/k_i, & i = j,\end{cases} \tag{A17}$$

$$(B)_{il} = \frac{k_1 - k_2}{k_1 + k_2}\times\begin{cases}\dfrac{(\mathbf{r}_i - \mathbf{r}_l)\cdot\mathbf{S}_i}{2\pi|\mathbf{r}_i - \mathbf{r}_l|^3}, & i\neq l,\\ 1, & i = l.\end{cases} \tag{A18}$$

2. Normalization of polarization charge

Discretizing the interface with the polarization charge poses some problems and we must take special care to ensure charge conservation; we therefore utilize Gauss' law to impose charge conservation for the system. The interface S is a closed surface; Gauss' law states

$$\int_S \frac{q_j(\mathbf{r} - \mathbf{r}_j)\cdot d\mathbf{S}}{4\pi k_j\epsilon_0|\mathbf{r} - \mathbf{r}_j|^3} = \begin{cases} q_j/k_j\epsilon_0 & \text{for } \mathbf{r}_j \text{ inside } S,\\ 0 & \text{for } \mathbf{r}_j \text{ outside } S.\end{cases} \tag{A19}$$

Discretizing Gauss' law, we get

$$\sum_{i\neq j}\frac{q_j(\mathbf{r} - \mathbf{r}_j)\cdot\mathbf{S}_i}{4\pi k_j\epsilon_0|\mathbf{r} - \mathbf{r}_j|^3} + \frac{q_j}{2k_j\epsilon_0} = \begin{cases} q_j/k_j\epsilon_0 & \text{for } \mathbf{r}_j \text{ inside } S,\\ 0 & \text{for } \mathbf{r}_j \text{ outside } S.\end{cases} \tag{A20}$$

This can be applied to A:

$$\sum_i (A)_{ij} = Q_j \equiv \begin{cases}\dfrac{2(k_1 - k_2)}{k_j(k_1 + k_2)}, & \mathbf{r}_j \text{ inside } S,\\ 0, & \mathbf{r}_j \text{ outside } S.\end{cases} \tag{A21}$$

For each point charge, we enforce Gauss' law by creating a normalized matrix

$$(A_N)_{ij} \equiv (A)_{ij} + \frac{Q_j - \sum_l (A)_{lj}}{\sum_l |(A)_{lj}|}|(A)_{ij}|. \tag{A22}$$

For point charges on surface sites, we assign half of the charge to be inside and half outside. We perform the same normalization on B; however, here we consider the charge at each site to be part of the surface and exactly half the flux of the charge goes through the rest of the surface S, resulting in

$$Q_j = \frac{k_1 - k_2}{k_1 + k_2}, \quad j \text{ surface site}. \tag{A23}$$

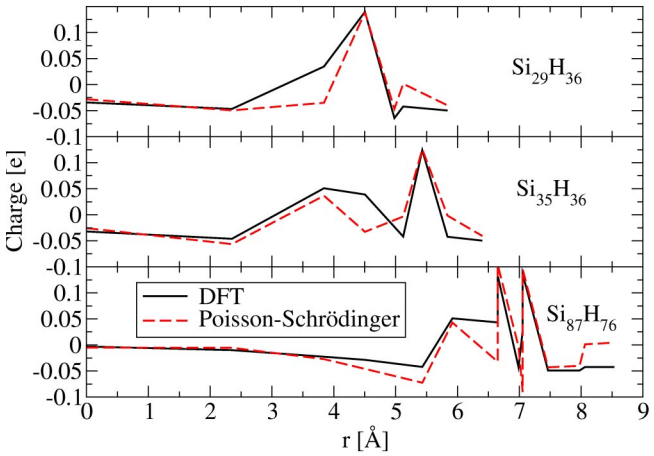

FIG. 8. (Color online) Charge on each site in three small approximately spherical hydrogen-terminated silicon crystals, as a function of the site radial coordinates. The solid line shows charge, calculated using *ab initio* density functional theory and natural population, multiplied by 0.4. The dashed line shows Mulliken charge for the current Poisson-Schrödinger model with the fitted parameters for hydrogen.

3. Calculating the potential

The potential at each site is calculated by summing the Coulomb potential from all other sites; for surface sites, we also include the on-site polarization charge by assuming it is spread over a circular disk with area S_i,

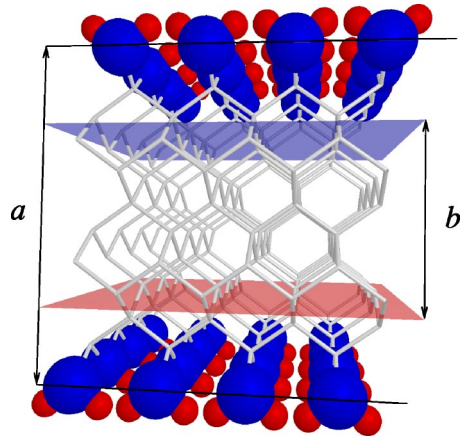

FIG. 9. (Color online) Geometry for calculation of the dielectric constant. The crystal is infinite in the x-y plane. The two charge planes are placed halfway between two (100) atomic planes, chosen so that the $b \approx a/2$. The surface is hydrogen terminated. The radius of each sphere is proportional to the charge on the site. The on-site charge is small everywhere except on the surface sites, which are positive, and the hydrogen sites, which are negative.

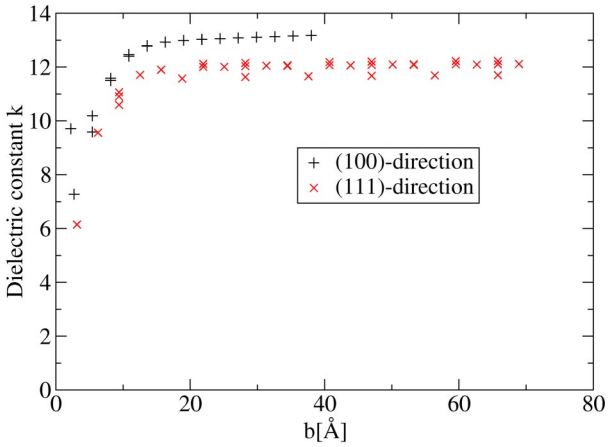

FIG. 10. (Color online) The dielectric constant for Si the model for surfaces normal to the (100) and (111) directions, between two charge planes, separated by distance b. The effective dielectric constant for core polarization used is $k_c=3.0$.

$$V_i = \sum_{j\neq i} \frac{q_j/k_j + q_j^{pol}}{4\pi\epsilon_0|\mathbf{r}_i - \mathbf{r}_j|} + \frac{q_i^{pol}}{2\epsilon_0\sqrt{\pi S_i}}, \tag{A24}$$

given that the potential at the center of a homogeneously charged circular disk of radius r is $V=q/2\epsilon_0\pi r$, where q is the charge.

4. Surface of a structure

We are considering crystalline structures of silicon where each atom is bound to four neighbors. We define a surface site to be a site with less than four neighbors. This leaves us with three cases for surfaces sites.

(i) *Three neighbors*. We set the surface normal to be pointing in the direction of the missing neighbor. The area of the surface site is set to $S_l=45.54$ a.u.^{2}; this is the correct area for each site on a (111) surface, where all surface atoms have exactly one missing neighbor.

(ii) *Two neighbors*. We set the surface normal to be pointing in a central direction between the two missing neighbors. The area of the surface site is set to $S_l=52.66$ a.u.^{2}; this is the correct area for each site on a (100) surface, where all surface atoms have exactly two missing neighbors.

(iii) *One neighbor*. None of the structures considered have this surface configuration.

APPENDIX B: FITTING OF PARAMETERS

1. Hydrogen

We obtained parameters for hydrogen by fitting to *ab initio* density functional calculations,[21] for a small approximately spherical hydrogen-terminated silicon crystal ($Si_{87}H_{76}$). The Mulliken charge calculations, used in our model, produce smaller charges than natural orbital calculations, used in the DFT calculations. We have therefore chosen to fit our Mulliken charge calculations to 40% of the natural orbital DFT charge.

The fit is shown in Fig. 8. The parameters fitted were the value 0.232 Ry in Eq. (5) for the on-site potential and the hopping parameters $S_s=-0.49$ Ry, $S_p=-0.23$ Ry, and $S_d=0$ Ry in Eq. (6). The hydrogen orbitals are assumed to be orthogonal to the silicon orbitals; allowing nonzero overlap does not improve the fit noticeably.

2. Aluminum and phosphorus

Aluminum and phosphorus are isoelectronic with silicon, so we use the same hopping and overlap parameters as for silicon. The on-site Hamiltonian parameters for Al and P are based on VOIE data (see Table I) for the charge and occupation dependence [see Eq. (1)]. The parameters B_l parameters in Eq. (1) have been fitted to show a crossover for the charge on the dopant site and reasonable values for dopant-level energies for the largest nanocrystals considered. The parameters are, for aluminum, $B_s=-0.091\,984\,9$ Ry, $B_p=0.576\,522$ Ry, and $B_d=1.155\,28$ Ry, and for phosphorus, $B_s=-0.586\,838$ Ry, $B_p=0.212\,551$ Ry, and $B_d=1.008\,22$ Ry.

3. Dielectric constant

The theory for electrostatic interaction (Appendix A) contains one fitting parameter—i.e., the susceptibility of the core electrons expressed as a dielectric constant k_c. The value of $k_c=3.0$ was decided by calculating the polarization charge in the model, due to two charge planes with charge sheet densities σ and $-\sigma$ inserted into an infinite slab of silicon. See Fig. 9 for computations in the (100) direction; the (111)-direction computations are treated analogously. The total dielectric constant k is calculated as

$$k = \frac{\sigma}{\sigma_{\text{net}}}, \tag{B1}$$

where σ_{net} is the shielded net charge in the top half of the slab, obtained by adding the applied charge, the charge of the valence electrons, the charge of the nuclei with core electrons, and the polarization charges of the core electrons, in the same way as in Appendix A. Figure 10 shows how the dielectric constant of the model changes when the thickness of the silicon slab and distance between the two charge planes charge are increased. We see a slight anisotropy in the model, but the dielectric constant k is near the experimental value 11.8.

*Electronic address: tblomqui@sfu.ca
†Electronic address: kirczeno@sfu.ca

[1] G. E. Moore, Electronics **38**(8), 114 (1965).
[2] M. Lannoo and J. Bourgoin, *Point Defects in Semiconductors II* (Springer-Verlag, Berlin, 1983).
[3] C. Kittel, *Introduction to Solid State Physics*, 7th ed. (Wiley, New York, 1996).
[4] W. Kohn and J. M. Luttinger, Phys. Rev. **97**, 1721 (1955); **98**, 915 (1955).
[5] C. Kittel and A. H. Mitchell, Phys. Rev. **96**, 1488 (1954).
[6] M. Lannoo and J. Bourgoin, *Point Defects in Semiconductors I* (Springer-Verlag, Berlin, 1981).
[7] M. Altarelli, W. Y. Hsu, and R. A. Sabatini, J. Phys. C **10**, L605 (1977).
[8] L. Resca, R. Resta, and H. B. Shore, Phys. Rev. B **25**, 4031 (1982).
[9] D. J. Lohrmann, L. Resca, G. P. Parravicini, and R. D. Graft, Phys. Rev. B **40**, 8404 (1989); **40**, 8410 (1989).
[10] W. Kohn, Phys. Rev. **105**, 509 (1957).
[11] A. Mimura, M. Fujii, S. Hayashi, D. Kovalev, and F. Koch, Phys. Rev. B **62**, 12625 (2000).
[12] D. V. Melnikov and J. R. Chelikowsky, Phys. Rev. Lett. **92**, 046802 (2004).
[13] M. Lannoo, C. Delerue, and G. Allan, Phys. Rev. Lett. **74**, 3415 (1995).
[14] J.-L. Zhu, J.-J. Xiong, and B.-L. Gu, Phys. Rev. B **41**, 6001 (1990).
[15] B. Stébé, E. Assaid, F. Dujardin, and S. Le Goff, Phys. Rev. B **54**, 17785 (1996).
[16] R. K. Pandey, M. K. Harbola, and V. A. Singh, J. Phys.: Condens. Matter **16**, 1769 (2004).
[17] G. T. Einevoll and Y.-C. Chang, Phys. Rev. B **40**, 9683 (1989).
[18] S. Estreicher, Phys. Rev. B **37**, 858 (1988).
[19] Z. Zhou, R. A. Friesner, and L. Brus, J. Am. Chem. Soc. **125**, 15 599 (2003).
[20] H. S. Stoker, *Introduction to Chemical Principles*, 4th ed. (Macmillan, New York, 1993).
[21] We employed the GAUSSIAN 98 numerical implementation of density functional theory with the 6-31G(d) basis set and the B3LYP exchange-correlation energy functional.
[22] A. E. Reed, L. A. Curtiss, and F. Weinhold, Chem. Rev. (Washington, D.C.) **88**, 899 (1988).
[23] J. R. Chelikowsky, L. Kronik, and I. Vasiliev, J. Phys.: Condens. Matter **15**, R1517 (2003).
[24] D. Kovalev, H. Heckler, G. Polisski, and F. Koch, Phys. Status Solidi A **215**, 871 (1999).
[25] N. Bernstein, M. J. Mehl, D. A. Papaconstantopoulos, N. I. Papanicolaou, M. Z. Bazant, and E. Kaxiras, Phys. Rev. B **62**, 4477 (2000); **65**, 249902(E) (2002).
[26] S. P. McGlynn, L. G. Vanquickenborne, M. Kinoshita, and D. G. Carroll, *Introduction to Applied Quantum Chemistry* (Holt, Rinehart and Winston, Inc, New York, 1972).
[27] There is an error in Eq. (5) in Ref. 25; the correct expression is given here.
[28] W. A. Harrison, *Electronic Structure and the Properties of Solids* (Dover, New York, 1989).
[29] O. Madelung, *Semiconductors Group IV Elements and III-V Compounds* (Springer-Verlag, Berlin, 1991).
[30] L. Liu, C. S. Jayanthi, and S.-Y. Wu, J. Appl. Phys. **90**, 4143 (2001).
[31] K. Yokoyama, T. Ochi, A. Yoshimoto, Y. Sugawara, and S. Morita, Jpn. J. Appl. Phys., Part 2 **39**, L113 (2000).
[32] A. Zunger and L.-W. Wang, Appl. Surf. Sci. **102**, 350 (1996).
[33] B. Delley and E. F. Steigmeier, Phys. Rev. B **47**, 1397 (1993); Appl. Phys. Lett. **67**, 2370 (1995).
[34] S. Öğüt, J. R. Chelikowsky, and S. G. Louie, Phys. Rev. Lett. **79**, 1770 (1997).
[35] A. J. Williamson, J. C. Grossman, R. Q. Hood, A. Puzder, and G. Galli, Phys. Rev. Lett. **89**, 196803 (2002).
[36] A preliminary study based on an early version of the model has been reported in T. Blomquist and G. Kirszenow, Nano Lett. **4**, 2251 (2004).
[37] J. D. Jackson, *Classical Electrodynamics*, 3rd ed. (Wiley, New York, 1999).